MIT Open Access Articles

Hitomi Constraints on the 3.5 keV Line in the Perseus Galaxy Cluster

CrossMark

Hitomi Constraints on the 3.5 keV Line in the Perseus Galaxy Cluster

Hitomi Collaboration[*]

(See the end matter for the full author and affiliation lists.)

Abstract

High-resolution X-ray spectroscopy with *Hitomi* was expected to resolve the origin of the faint unidentified $E \approx 3.5$ keV emission line reported in several low-resolution studies of various massive systems, such as galaxies and clusters, including the Perseus cluster. We have analyzed the *Hitomi* first-light observation of the Perseus cluster. The emission line expected for Perseus based on the *XMM-Newton* signal from the large cluster sample under the dark matter decay scenario is too faint to be detectable in the *Hitomi* data. However, the previously reported 3.5 keV flux from Perseus was anomalously high compared to the sample-based prediction. We find no unidentified line at the reported high flux level. Taking into account the *XMM* measurement uncertainties for this region, the inconsistency with *Hitomi* is at a 99% significance for a broad dark matter line and at 99.7% for a narrow line from the gas. We do not find anomalously high fluxes of the nearby faint K line or the Ar satellite line that were proposed as explanations for the earlier 3.5 keV detections. We do find a hint of a broad excess near the energies of high-*n* transitions of S XVI ($E \simeq 3.44$ keV rest-frame)—a possible signature of charge exchange in the molecular nebula and another proposed explanation for the unidentified line. While its energy is consistent with *XMM* pn detections, it is unlikely to explain the MOS signal. A confirmation of this interesting feature has to wait for a more sensitive observation with a future calorimeter experiment.

Key words: dark matter – galaxies: clusters: individual (A426) – galaxies: clusters: intracluster medium – X-rays: galaxies: clusters

1. Introduction

The nature of dark matter (DM) is one of the fundamental unsolved problems in physics and astronomy. Direct particle searches in laboratories as well as searches for electromagnetic signal from celestial objects have been conducted with no unambiguous detection so far. X-ray observations of DM concentrations, such as galaxies and clusters, provide a probe for a particular DM candidate, a sterile neutrino, which is predicted to decay and emit an X-ray line (Dodelson & Widrow 1994; Abazajian et al. 2001). Early searches that provided upper limits on line flux (and thus the particle decay rate) as a function of line energy (which gives the particle mass) are reviewed, e.g., in Abazajian et al. (2012) and Boyarsky et al. (2012).

A possible detection was reported by Bulbul et al. (2014, hereafter B14), who found an unidentified line at $E \approx 3.55$ keV in the stacked spectrum of a large sample of galaxy clusters using *XMM-Newton* EPIC MOS and pn. Within their sample was the Perseus cluster (its central region), whose signal was particularly strong. B14 also reported a detection from Perseus with *Chandra* at the same energy. Boyarsky et al. (2014) reported an *XMM* detection in the outer region of Perseus. Urban et al. (2015) and Franse et al. (2016, hereafter F16) detected the line in several regions of Perseus with *Suzaku*; however, Tamura et al. (2015) did not detect it in the same *Suzaku* data. The 3.5 keV line was also reported from other objects, such as the Galactic Center (Boyarsky et al. 2015) and M31 (Boyarsky et al. 2014). Other sensitive searches did not detect a significant line signal (e.g., from the Milky Way halo, Sekiya et al. 2016; Draco dwarf, Ruchayskiy

et al. 2016; stacked *Suzaku* clusters, Bulbul et al. 2016). Some of the nondetections were inconsistent with other detections under the decaying DM hypothesis (in which the line flux must be proportional to the projected DM mass), most significantly, in a sample of galaxies (Anderson et al. 2015). We also note here that the signal from Perseus reported by *XMM*, *Chandra*, and *Suzaku* was higher than expected given the signal from the rest of the cluster sample (B14). Astrophysical explanations of the reported line, in addition to those considered by B14, have also been proposed; a critical review can be found in F16. An extensive review of the recent observations is given, e.g., by Iakubovskyi (2015).

As recognized in all previous studies, the above line detections were near the capability for CCD detectors—for a ∼100 eV resolution, the line reported from clusters with a ∼1 eV equivalent width (EW) is a 1% bump above the continuum, easily affected by errors in modeling the nearby atomic lines and in instrument calibration. A confirmation with a much better spectral resolution was considered essential. *Hitomi*, launched in 2016 February and lost in March (Takahashi et al. 2014, 2016) after having returned a groundbreaking spectrum of the Perseus cluster (Hitomi Collaboration 2016, hereafter H16), offered us such a possibility. We present results from this data set below.

We use $h = 0.7$, $\Omega_m = 0.3$, and $\Omega_\Lambda = 0.7$ cosmology. The cluster heliocentric redshift (average for member galaxies) is 0.0179 (Strubble & Rood 1999), and the redshift in the CMB frame is 0.01737, which gives $d_L = 75.4$ Mpc and a scale of 21.2 kpc per 1′. We use the 68% (1σ) confidence level for errors unless stated otherwise.

2. Data

The Perseus cluster was the first-light target for *Hitomi*, observed early in the instrument activation phase with the Soft

* Corresponding authors: M. Markevitch, C. Kilbourne, and T. Tamura (maxim.markevitch@nasa.gov, caroline.a.kilbourne@nasa.gov, tamura.takayuki@jaxa.jp)

X-Ray Spectrometer (SXS; Kelley et al. 2016). SXS is an array of 35 calorimeter pixels with a 4.9 eV FWHM energy resolution (H16), covering a $3' \times 3'$ field of view (FOV) at the focus of a Soft X-Ray Telescope (SXT; Soong et al. 2014; Okajima et al. 2016). To maximize statistics, here we coadd the 230 ks Perseus data set used in H16 and a later 45 ks pointing for a total exposure of 275 ks. The former data set is a combination of observations 2 on 2016 February 24–25 and 3 on March 3–5, both pointed $\sim 1'$ away from the cluster center, while the latter (observation 4 on March 6–7) is on-center. The earliest observation, observation 1, was pointed away from the core and is not included.

For these observations, SXS was still protected from possible contaminants by the closed gate valve (GV) window. It includes a Be filter that absorbs soft X-ray photons. At $E = 3.5$ keV, the GV window transmission is $1/4$ of that in the normal operation mode, yielding the number of photons equivalent to about 70 ks of normal observations.

3. Analysis

To fully utilize the SXS high energy resolution, accurate calibration of gain (the conversion from the amplitude of the detected signal to photon energy) for each of its 35 pixels is essential. Unfortunately, the individual pixel gains were changing during the early part of the mission, and a contemporaneous gain calibration for the SXS array as planned for later operations was not available. The procedure that we devised to calibrate the Perseus data is described in H16. For some of the analysis in H16, an additional scale factor was applied to force the bright 6.7 keV Fe Heα line from the cluster to appear at the same energy in every pixel. This additional step removes the true gas velocity gradient across the cluster along with any residual gain errors. Since DM does not move with the gas, this would also broaden a DM emission line. However, as reported in H16, the gas velocity difference across the Perseus core is around 150 km s^{-1}, much less than the expected width of the DM line that we will try to detect. We use the energy-aligned data in this work, but have confirmed that our results are essentially the same with or without this final energy-scale alignment. We do not report the best-fit redshift below because we simply recover the value used for energy alignment.

We used the Be layer thickness ($270 \pm 10 \mu m$) calibrated using Crab and G21.5–0.9 spectra taken after the Perseus observation.[78] This differs from the instrument response used in H16 and results in a more reliable slope of the spectrum in the 3–7 keV band.

The detector energy response (RMF) was generated using the observed energy resolution of the individual pixels. Its uncertainty is discussed in H16 and is negligible for this work. We bin the spectrum by 2 eV (which is close to optimal binning; Kaastra & Bleeker 2016) and fit using the C-statistic (Cash 1979). The number of counts per 2 eV bin is around 200 in this band, i.e., the statistics is nearly a Gaussian distribution with $\sigma = \sqrt{N}$. The instrumental background is negligible.

3.1. Systematic Uncertainties

The SXT has a $1.'2$ angular resolution (half-power diameter). For our analysis of the spectrum from the whole $3' \times 3'$ FOV,

we do not attempt to account for PSF scattering in and out of the FOV, and use the instrument response for an on-axis point source. We estimate the effect of this simplification on the model normalization to be $\sim 10\%$.

The uncertainty of the Be layer thickness in the GV window, $\pm 10 \mu m$, corresponds to a $\pm 2.5\%$ uncertainty for the flux at $E = 3.5$ keV.

A more insidious effect may be caused by uncertainty in modeling the SXT effective area (Kurashima et al. 2016). The SXT reflectivity around the Au M edges was measured on the ground and combined with values from Henke et al. (1993) for other energies. The ground measurements show $\sim 1\%$ systematic deviations from Henke, one of which is in the 3.43–3.68 keV interval above the Au M1 edge—at our energies of interest. Given the finite accuracy of the ground measurements, we consider the possibility that the Henke values are more accurate. To quantify the effect of this uncertainty, below we will derive some of the results using both the default area curve (which uses the *Hitomi* mirror measured reflectivities) and one in which the Henke values were used above the Au M1 edge. Similar deviations may be seen at other Au M edges, but the next one (M2 at 3.15 keV) is well outside our interval of interest and we will not consider it.

4. Results

4.1. The ICM Model

We fit the full-FOV Perseus spectrum with a BAPEC thermal plasma model (AtomDB 3.0.3beta2; Foster et al. 2012) with elemental abundances relative to Lodders (2003). We fix the Galactic absorption at $N_H = 1.38 \times 10^{21}$ cm^{-2} (Kalberla et al. 2005), which agrees with that derived in the X-ray by *Chandra* (Schmidt et al. 2002) and *XMM* (Churazov et al. 2003). A broadband SXS spectrum requires a power-law component from the AGN in NGC 1275 (Fabian et al. 2015). The SXS broadband effective area calibration is not yet good enough for fitting multiple continuum components reliably. Therefore, to derive a spectral shape for the AGN component, we extracted the AGN spectrum from the off-center *Chandra* Perseus observations (those where the point-like AGN is not affected by pileup) and obtained a power-law photon slope $\alpha = -1.8$ (defined as $S_X \propto E^\alpha$) and an absorption column (Galactic plus intrinsic) of 3.3×10^{21} cm^{-2}. We included a component of this shape along with the thermal model and fit the SXS spectrum in the 3–7 keV band, obtaining a normalization for the AGN component of 9.0×10^{-3} phot cm^{-2} s^{-1} keV^{-1} at $E = 1$ keV. We fix it in the subsequent fits and leave further discussion of the AGN spectrum for future work. Its contribution to the 3–4 keV flux is 15%, and it does not affect our results.

The 2.85–4.1 keV spectrum with the best-fit model is shown in Figure 1. This energy interval is chosen to include all the interesting lines but avoid the effective area uncertainty sharply increasing at lower energies. The BAPEC model parameters for a fit in this band are $kT = 3.48 \pm 0.07$ keV, an abundance of 0.54 ± 0.03 solar, and the line of sight (los) velocity dispersion of 179 ± 16 km s^{-1} (which becomes 197 ± 16 km s^{-1} without the pixel energy alignment). The fit is formally good with C-statistic of 603 ($\chi^2 = 611$) for 619 dof. If the power-law component is omitted, the temperature changes to 3.70 ± 0.07 keV and abundance to 0.48 ± 0.02.

---

[78] heasarc.gsfc.nasa.gov/docs/hitomi/calib/hitomi_caldb_docs.html

The parameters obtained from a fit in this narrow interval are qualitatively similar to those from a broader 3–7 keV band with the power-law slope fixed at -1.8, which gives $kT = 3.84 \pm 0.02$ keV (though with a considerably higher abundance, 0.68 ± 0.01, now dominated by Fe lines). The closeness of the best-fit temperatures, even though they are statistically inconsistent, suggests that the shape of the effective area curve over the 3–7 keV band is reasonably correct. Importantly for this work, the continuum model at the energy of interest (3.5 keV) differs by only 1% between the above fits. We further checked its robustness by fitting a simple power law in the interval 3.30–3.75 keV between the bright Ar and Ca lines, excluding intervals with all the weak model lines between, and obtained a continuum flux only 0.4% different from our default BAPEC model. As a further check, we also compared the best-fit normalization of our BAPEC model to that from *Chandra* for the same region of the cluster, excluding the AGN. Our normalization is $\sim$10% below *Chandra*'s, which is a good agreement, given the preliminary calibration and the simplified accounting for the PSF.

As seen in Figure 1, lines from all elements are fit surprisingly well with a simple single-temperature, single-abundance model. Some possible faint lines (K XVIII Heα, Ar XVII Heβ, K XIX Lyα) may show problems with line energies, but none of these lines is a significant detection. Line identifications and individual abundances will be addressed in a future work.

4.2. Constraint on the Previously Reported 3.5 keV Line

The red and blue brackets in Figure 1 show 90% confidence intervals for the 3.5 keV line energy for the most sensitive measurement of B14, that of the *XMM* MOS stacked-cluster sample, and for the *XMM* MOS spectum of the Perseus region covered by *Hitomi*. For a quantitative comparison, we extracted a MOS 1 + 2 spectrum from a circular region approximating the SXS FOV (both offset and solid angle) in observations 2 and 3 that give most of the exposure, ignoring a small offset for observation 4. We then modeled the 3.5 keV line in that spectrum reproducing the procedure in B14. In particular, we fit the MOS spectrum in the 2.4–6 keV band using a line-free single-temperature APEC model and a set of Gaussian lines at energies of the known atomic lines (with energies allowed to vary slightly), in order to model the continuum and lines in as model-independent a way as possible given a CCD detector. The faint atomic lines near the energy of interest that could not be directly detected by the CCD, namely, K XVIII Heα at 3.51 keV (rest-frame) and Ar XVII Heβ satellite at 3.62 keV, were constrained in the fit using the bright lines of S XV Heα (2.46 keV rest) and S XVI Lyα (2.62 keV), which are good temperature diagnostics. The measured S XV and S XVI fluxes are $(9.0 \pm 1.2) \times 10^{-5}$ and $(2.15 \pm 0.05) \times 10^{-4}$ phot s^{-1} cm^{-2}, respectively. A ratio of these lines corresponds to a temperature of 2.9 keV. We predicted the K line flux using this temperature (which is the relevant one, since K and Ar are likely to come from the same gas phase that dominates the S lines) and the S line fluxes, assuming the same abundances. The K XVIII is a triplet (3.47, 3.49, 3.51 keV) with a known flux ratio for its components (1:0.5:2.3). This resulted in an estimate for the K XVIII line at 3.51 keV of 2.0×10^{-6} phot s^{-1} cm^{-2}. We then allowed this flux to vary during the fit in the range 0.1–3 times the estimated flux, capping at 6×10^{-6} phot s^{-1} cm^{-2}, to account for possible temperature and abundance variations. The

Ar XVII satellite line is estimated from the measured Ar XVII Heα line at 3.12 keV, $(6.0 \pm 0.3) \times 10^{-5}$ phot s^{-1} cm^{-2}, and the Ar XVII resonant/satellite line ratio for the above-determined temperature; the predicted Ar satellite line flux was 2.1×10^{-7} phot s^{-1} cm^{-2}, and we again allowed this flux to vary by factor 0.1–3 in the fit, capping at 6.3×10^{-7} phot s^{-1} cm^{-2}.

For the unidentified line, we obtained $f = (9.0 \pm 2.9) \times 10^{-6}$ phot s^{-1} cm^{-2} and $E = 3.54^{+0.03}_{-0.04}$ keV (similar for the different assumed line widths from the interesting range). This is very close to the flux shown in Figure 15 of B14, which gives their *Astro-H* prediction, and is consistent with (but has a much smaller error than) the difference between the whole-Perseus flux and the one with the central $r = 1'$ region excised, given in their Table 5.

We first check how the flux caps for the K XVIII and Ar XVII satellite lines estimated for the MOS fit compare with the actual fluxes of those lines in the SXS spectrum. None of the lines is significantly detected; the flux of the possible blend of K XVIII Heα and ClXVII Lyβ (at 3.45 keV observed) is $(4.6 \pm 2.6) \times 10^{-6}$ phot s^{-1} cm^{-2}—under the K XVIII cap used for the MOS fit. The Ar XVII satellite flux (3.556 keV observed) is $(1.5 \pm 1.4) \times 10^{-6}$ phot s^{-1} cm^{-2}, consistent with the cap. The above MOS flux of the 3.5 keV feature is *in excess* of these caps, but even if these faint lines were completely ignored in the MOS fit, neither of them approaches the derived 3.5 keV flux, excluding one of the astrophysical explanations proposed in B14.

The MOS fluxes of the S XV Heα and S XVI Lyα lines, used to derive the K cap, are consistent with the *Hitomi* fluxes, once the relatively small contribution of Si XIV Lyγ blending with S XV Heα is added. The Ar XVII Heα MOS-derived flux is consistent with the blend of this line and a $\sim$2$\times$ stronger S XVI Lyβ line, resolved in the *Hitomi* spectrum (Figure 1); this blending was ignored in the MOS analysis (as in B14) and resulted in a conservatively high cap on the Ar satellite line. A more detailed comparison of the *XMM* and *Hitomi* line fluxes will be given in a future paper.

We start checking the consistency of the MOS-derived 3.5 keV emission line with the SXS spectrum by adding a Gaussian line with this flux at a range of energies to the SXS model. We consider an astrophysical line broadened by turbulence or a wider line expected from the DM decay. If the astrophysical line comes from an element whose lines are seen in this range, thermal broadening would correspond to 100 km s^{-1}. Added in quadrature with turbulent broadening of 180 km s^{-1}, this results in an intrinsic Gaussian $\sigma = 2.4$ eV at these energies (in addition to the instrumental $\sigma = 2.1$ eV, or 4.9 eV FWHM, modeled by the RMF). For a DM line, we try 1300 km s^{-1} ($\sigma = 15$ eV), which is the los velocity dispersion of the cluster galaxies (Kent & Sargent 1983). An arbitrary intermediate case of 800 km s^{-1} corresponds to a lower dispersion in the region of the cD galaxy projected onto the cluster dispersion. The additional broadening for a putative DM line caused by our energy alignment (Section 3) is negligible for such widths, and it would not apply to the narrow line originating in the gas.

Figure 2 shows the value of ΔC (which has the same interpretation and normalization as $\Delta \chi^2$) for the addition of a line at the best-fit MOS flux, compared to the best-fit SXS line flux at that energy (allowing for negative line flux to avoid distorting the probability distribution, as advised by Protassov et al. 2002). For the broad line, we also show ΔC for a
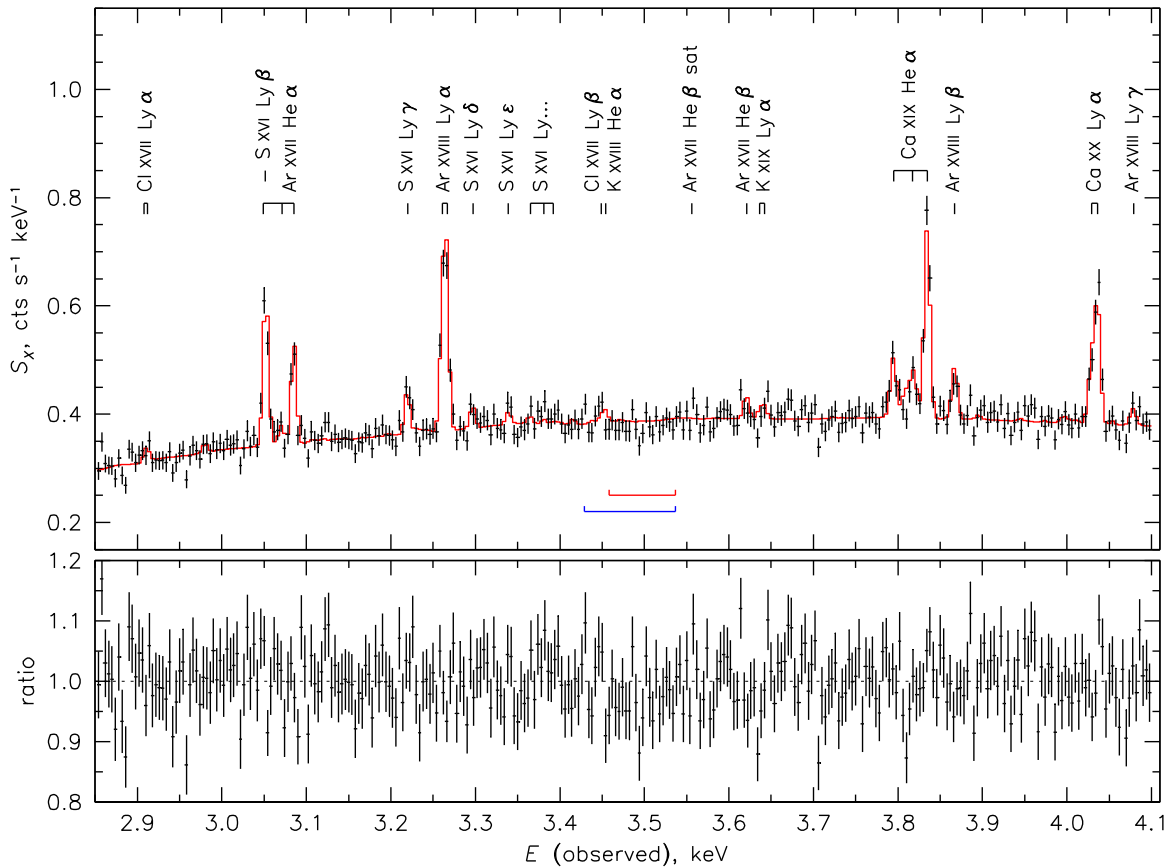
Figure 1. SXS spectrum from the whole field of view, combining three pointings. Energy is in the observer frame; bins are 4 eV for clarity (2 eV bins were used for fitting). Vertical error bars are 1σ Poisson uncertainties in each bin; horizontal error bars denote the bins. Red curve is a best-fit BAPEC model with $kT = 3.5$ keV, abundances of 0.54 solar (same for all elements), los velocity dispersion of 180 km s^{-1}, and a power-law component as required by a fit in a broader band (see the text). Prominent atomic lines seen in the model (identified using AtomDB) are marked, along with the interesting Ar XVII satellite line (B14) that's too faint to be seen in the model. Brackets show 90% confidence intervals on the unidentified 3.5 keV line energy for the most-restrictive XMM MOS stacked-clusters sample in B14 (red) and for the XMM MOS Perseus spectrum from the region covered by the SXS (blue).

reference model with zero line flux rather than the best-fit SXS flux. B14's most-restrictive 90% MOS energy interval for the stacked sample is shown, since we are assuming that this is a DM line and it has the same energy in all objects. For narrow and broad lines, the best-fit *XMM* MOS flux value is inconsistent with the SXS spectrum; the weakest constraint is for the broad line and the discrepancy is at least $\Delta C = 12$. Using only observations $2 + 3$ (excluding the better-centered, but short observation 4) reduced ΔC for the broad line compared to the zero-flux model by about 4, commensurate with the reduction in the number of photons. The effective area uncertainty described in Section 3.1 is illustrated by error bars for the broad line; the alternative area curve reduces the model values at these energies slightly, thereby reducing the significance of the exclusion of the *XMM* flux to at least $\Delta C = 9$. Its effect on the narrower lines is weaker.

4.2.1. The Statistical Question

To interpret the above ΔC (or $\Delta \chi^2$) in terms of a confidence level for the line exclusion, we should note that the statistical question we are asking—what is the confidence level of excluding the previously detected line—is different from a blind line search employed for detecting the line. If a spectral line is detected in a blind search and it corresponds, e.g., to a 3σ deviation, one has to estimate the probability of a false detection under the hypothesis of no line, caused by a positive

random fluctuation. Because a $+3\sigma$ deviation appearing at *any* spectral bin would be detected as a line, such a probability is the probability of a $+3\sigma$ deviation in one bin times the number of bins where the line could be found within the searched interval (the "look-elsewhere" effect; e.g., Gross & Vitells 2010; this factor was applied in B14). However, here we must estimate the probability of a null hypothesis in which the line exists and we falsely reject it because of a random negative deviation at the position of the line. While -3σ deviations can appear at any spectral bin, only *one* of them, that happens in the bin with the line, would result in false rejection, while all others would be dismissed as mere random deviations. Thus, even though we do not know where within the *XMM* interval the line is, the probability of false rejection is the probability of a -3σ deviation in one bin—there is no look-elsewhere effect in our statistical problem. A $\Delta C = 9$ or $\Delta \chi^2 = 9$ corresponds to the standard one-parameter $1 - (1 - 0.997)/2 \approx 99.9\%$ confidence level. Because ΔC is not constant across the interval in Figure 2, we can take its minimum for a conservative limit for rejecting a certain line flux.

The above ΔC gives only the *Hitomi* statistical constraint and does not take into account the fact that the *XMM* SXS-FOV detection itself is only 3σ significant (and thus cannot be ruled out with a $>3\sigma$ significance). To answer a narrower question of how inconsistent the *Hitomi* and *XMM* MOS results for the
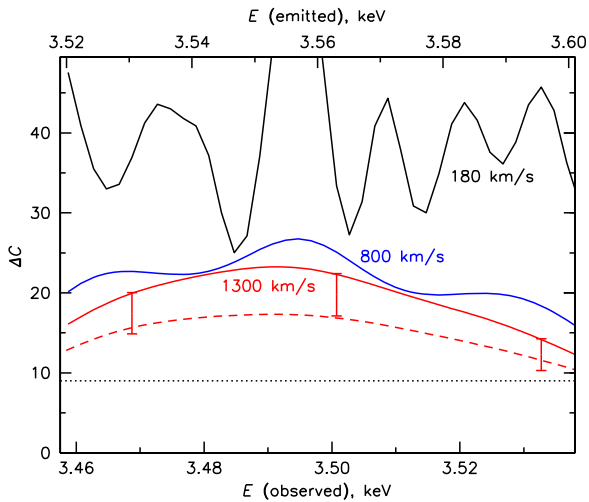
Figure 2. Difference of C-statistic between a model with a line with the best-fit *XMM* MOS flux (9×10^{-6} phot s^{-1} cm^{-2}) and the best-fit SXS flux (shown in Figure 3; flux is allowed to take negative values) as a function of line energy within the B14 most-restrictive confidence interval for the line. Curves for different line widths are shown (black: 180 km s^{-1}, blue: 800 km s^{-1}, red: 1300 km s^{-1}). For the 1300 km s^{-1} case, we also show ΔC between models with the *XMM* MOS line flux and zero line flux (red dashed line). Error bars illustrate a systematic uncertainty of the SXT effective area described in Section 3.1; its effect is most significant for the broad line and we do not show other cases for clarity. Dotted line is at $\Delta C = 9$, which corresponds to 3σ exclusion for Gaussian errors.

same region are, we ran a simple Monte Carlo simulation with the line energy and flux randomly drawn from the *XMM* one-parameter intervals assuming Gaussian distributions and the *Hitomi* line flux at that energy randomly drawn using the *Hitomi* statistical uncertainty. For a broad (1300 km s^{-1}) line, the SXS line flux was below the *XMM* flux in 99.2% of the trials for the default effective area, in 98.9% of the trials if we use the alternative area curve, or in 97.2% of the trials if we force the SXS line flux to be zero but use the same statistical errors. For a narrow (180 km s^{-1}) line, for which the *Hitomi* error is smaller, the discrepancy is at 99.7% for all three cases.

4.3. Broader Search

Figure 3 shows the best-fit SXS flux for the additional line as a function of energy, with upper and lower limits at $\Delta C = 9$ ($\pm 3\sigma$ for Gaussian distribution), for a narrow and broad line, as well as the conservative $+3\sigma$ limit selected from among the different line widths in this range. The figure shows a wider interval of possible interest that combines *XMM* MOS and pn 3σ line energy intervals. One notable feature is a broad negative "dip" in residuals at $E \approx 3.50$ keV (observed) of about 3%–4%, also noticeable in residuals in Figures 1 and 4. The model lines with different widths overplotted in Figure 4 show that a broad line may be affected but not a narrow line, as indeed seen in Figure 3. This deviation has a relatively low statistical significance ($\sim 2.3\sigma$). We have checked the SXS spectra of Crab and G21.5-0.9 (Figure 4; details will be given in forthcoming papers), both continuum sources well-fit with a simple power-law model in the energy range of interest. Neither source shows any comparable deviations at this energy. The Crab spectrum (shown binned to 32 eV, which roughly corresponds to the expected DM line width) has 1.5 times more counts at these energies than the Perseus spectrum, and has sufficient statistics to exclude any effective area artifact around
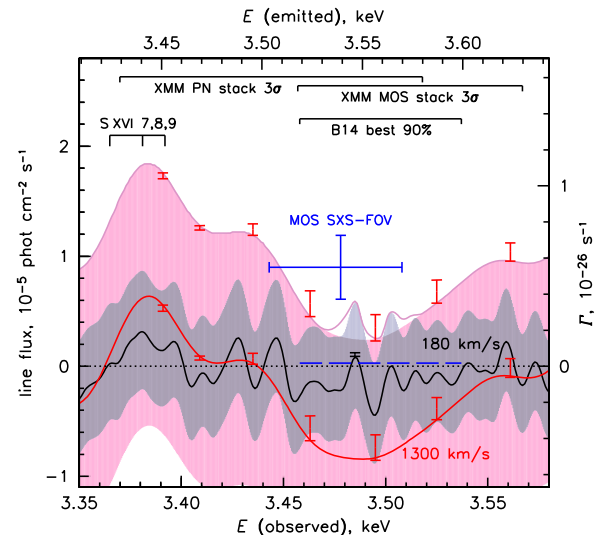

Figure 3. Best-fit line flux (solid curves) and the flux limits for $C_{\min} + 9$ ($\pm 3\sigma$; shaded bands) for an additional emission line as a function of energy. We show an interesting broad band encompassing *XMM* MOS and pn 3σ intervals for stacked-cluster samples from B14 (brackets at top). Black line with gray band (labeled 180 km s^{-1}) corresponds to a turbulent-broadened line; red line with pink band (1300 km s^{-1}) corresponds to a DM line. A magenta outline shows the highest flux limit from those for different widths in the 180–1300 km s^{-1} interval. Red and black error bars illustrate the systematic uncertainty of the effective area (Section 3.1), shown for the best-fit curve and the upper limit for the broad line. This effect is negligible for the narrow line, so only one location is shown. A line flux of 5×10^{-6} phot s^{-1} cm^{-2} corresponds to EW $\simeq 1$ eV. Blue cross shows the MOS detection for the SXS FOV with 1σ one-parameter uncertainties. Blue dashed line shows the expected flux based on the stacked-cluster signal (Section 5). Also shown for reference is the "B14 best" interval covered by Figure 2. The only interesting unmodeled positive deviation—though a low-significance one—is near the energies of the high-n transitions of S XVI, marked at top. The right vertical axis shows the approximate corresponding sterile neutrino decay rate Γ.

3.5 keV of much more than 1% (the size of the error bars). The area systematic uncertainty (Section 3.1), shown in the lower panel of Figure 4, is also a smaller (1%) effect. The fine structure of the Au M1 edge (same panel), measured with high energy resolution during ground calibration, occurs on energy scales smaller than the "dip."

We have also checked if this dip may be caused by some time-dependent instrumental effect. For this, we divided the full Perseus data set into the early and late subsets—observations 2 and 3 + 4, respectively, separated by a week (Section 2). Results from these subsets for the broadened line, analogous to those shown by the red line in Figure 3 for the full exposure, are shown in Figure 5. The dip appears in the early subset but not in the late one. However, the subsets are only $\sim 2\sigma$ apart at 3.5 keV, so the statistics are insufficient to determine if this is a systematic time-dependent change. The Crab observation (Figure 4) was performed later than our late subset and thus does not help in ruling out a transient instrumental artifact in earlier data; however, we cannot think of a physical explanation for such effect. Given the available data, we have to conclude that the dip is most likely an unfortunate statistical fluctuation and base our results on the whole data set in order to avoid statistical biases.

4.3.1. A Possible Excess at 3.44 keV (Rest-frame)

The only positive deviation in Figure 3 is a broad excess above the best-fit thermal model at $E = 3.38$–3.39 keV (observed). The statistical significance of this feature is only
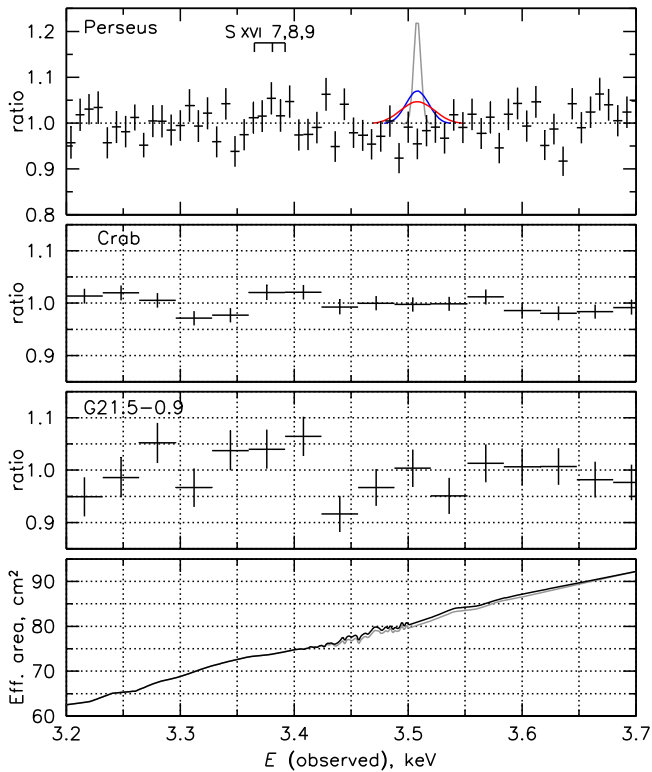
Figure 4. Ratios of data to best-fit models in the interesting energy range. Upper panel shows ratio of the same Perseus spectrum and model as in Figure 1, but binned by 8 eV. A line at 3.57 keV (rest-frame) with a flux derived by *XMM* in the SXS FOV (Section 4.2) is shown with curves of different colors, which denote different los velocity dispersions (gray: 180 km s^{-1}, blue: 800 km s^{-1}, red: 1300 km s^{-1}; see Section 4.2). Position of the potentially interesting S XVI feature (Section 4.3.1) is marked. Two middle panels show the residuals for power-law sources Crab and G21.5–0.9. The area modification (Section 3.1) is not included. The Crab spectrum has sufficient statistics to exclude a significant effective area artifact around 3.5 keV. Lower panel shows the effective area curve (gray line shows the modification from Section 3.1), including the fine structure above the Au M1 edge measured during ground calibration.
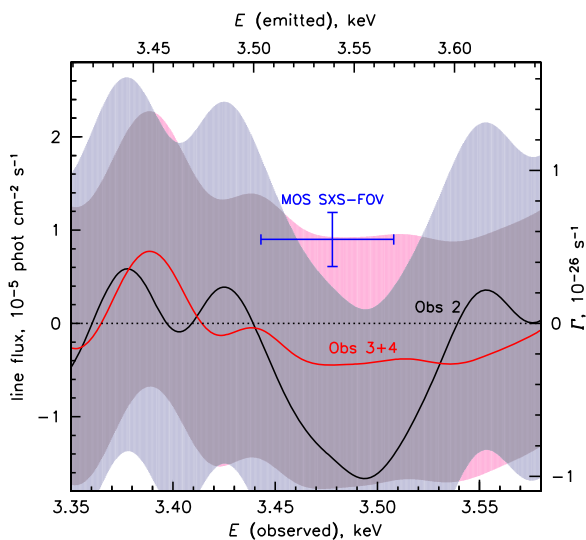
Figure 5. Best-fit flux (curves) and $\pm 3\sigma$ limits (shaded bands) for a 1300 km s^{-1} broadened line (similar to the red line and pink band in Figure 3), derived separately for the early subset ("Obs 2," black and gray) and later subset ("Obs 3 + 4," red and pink). The axes and the blue cross are the same as in Figure 3. The "dip" around 3.5 keV is present in the early subset and not in the late one, but the results are statistically consistent.

1.5σ and it would not be worth mentioning, if not for the fact that it is located at the energy of the high-n to $n = 1$ transitions of S XVI. Excess flux in these transitions can be interpreted as a signature of charge exchange between heavy nuclei coming in contact with neutral gas—possibly the molecular nebula observed in the Perseus core. These particular transitions were proposed as a possible explanation for the 3.5 keV line in clusters by Gu et al. (2015). A detection of charge exchange in the ICM would be of great astrophysical importance, but it should be confirmed with other elements (to be addressed in future work) and eventually with a longer exposure.

5. Discussion

Our analysis of the *Hitomi* spectrum of the Perseus cluster core reveals no unidentified emission line around the energy reported by B14. It is inconsistent with the presence of a line at the flux reported by B14 using *XMM* MOS (as rederived for the approximate SXS FOV). Taking into account the uncertainties of the *XMM* MOS measurement in this region, which itself is only 3σ significant, the inconsistency with *Hitomi* for a broad line (that would be emitted by DM) is at the 99% confidence level, and 99.7% for a narrow line from the ICM. The broad-line exclusion level is 97% if we force the SXS line flux to be zero, assuming in effect that the mild "dip" in the residuals (Section 4.3) is not statistical as we concluded, but some instrumental artifact present only in Perseus and not in other SXS data. We note here that F16, using *Suzaku* data for a similar Perseus region, reported a line flux and its uncertainty similar to that from the *XMM* SXS-FOV measurement, but given the lack of consensus between different *Suzaku* analyses (cf. Tamura et al. 2015), we leave a comparison with *Suzaku* for a later work.

We can exclude one of the 3.5 keV line astrophysical explanations proposed by B14—namely, anomalously bright K XVIII Heα or Ar XVII Heβ satellite lines. These lines are not significantly detected in the SXS spectrum, their fluxes are consistent with expectations and below the MOS 3.5 keV flux. If we consider a slightly wider energy range (Figure 3), there is a hint of a broad excess emission feature of the right amplitude (though at very low statistical significance) at $E \approx 3.44$ keV rest-frame, where charge exchange on S XVI has been predicted (Gu et al. 2015). However, the energy of this feature is 2.6σ (100 eV) away from the best-fit energy for the MOS SXS-FOV detection, and even more inconsistent with the MOS stacked-cluster sample, though it is consistent with the pn detections (B14). If confirmed with better statistics, it is an interesting feature in itself.

Given *Hitomi*'s much greater spectral resolution, it is likely that the inconsistency with *XMM* that we reported here is attributable to a systematic error in the *XMM* result. Possible causes will be examined in a future work, using the new accurate knowledge of the fluxes of all the nearby atomic lines from *Hitomi*, as well as *Suzaku* and *Chandra* spectra and models. One possible reason, mentioned among the Caveats in B14, is that with a CCD resolution, a spurious ~1% dip in the effective area curve is all that is needed to produce a false line-like residual of the observed amplitude (see Figure 7 in B14). This is an obvious problem for detections in a single object or in local objects, even when different instruments with similar low-resolution detectors are used. Such systematic effects can be minimized by stacking objects at different redshifts. In the cluster sample of B14, the 3.5 keV rest-frame

energy spans a 1.2 keV interval of detector energies, which should smear out any such instrument features. Thus, this systematic error will be much smaller in the stacked-sample signal.

As noted in B14 and subsequent works, the reported line in Perseus, and especially in its core, was much brighter than expected from the signal in the larger cluster sample, scaled by mass under the decaying DM hypothesis. Assuming that the high Perseus line flux is an artifact but the stacked-sample signal is real, we can evaluate the corresponding expected flux from the SXS FOV. To estimate the projected dark matter mass within this region, we use a total mass profile from Simionescu et al. (2011) and one from the Vikhlinin et al. (2006) $M - T$ scaling relation (the former was used in Urban et al. and the latter in B14), correcting them for the 14% baryon fraction. The projected DM mass within the SXS FOV is $(6–8) \times 10^{12} \, M_{\odot}$. For the sterile neutrino decay rate derived in B14 for the full cluster sample ($\Gamma \approx 2 \times 10^{-28} \, \mathrm{s}^{-1}$), we expect a 3.5 keV line with $f = (2.4–3.1) \times 10^{-7} \, \mathrm{phot \, s^{-1} \, cm^{-2}}$ (see, e.g., B14 for the equations), 30 times below the flux we ruled out above. This flux, shown by blue dashed line in Figure 3, is below the statistical noise in the current observation.

The right vertical axis in Figure 3 shows the sterile neutrino decay rate that corresponds to the line flux on the left axis, using the median of the projected DM mass estimates. The *Hitomi* 3σ upper limits on Γ are, unfortunately, much higher than many earlier constraints (see, e.g., B14). This is because of the high X-ray brightness of the ICM in the Perseus core, the short exposure (combined with the GV attenuation), and the small SXS FOV.

Our results from this relatively short observation illustrate the dramatic improvement in sensitivity for narrow features from that of CCD detectors. However, as expected, the improvement for a putative cluster DM line, which would have a width of 30–35 eV (FWHM), is less significant. The short *Hitomi* observation excluded the anomalously bright signal reported from the Perseus core. However, to test the much weaker stacked-sample detection (provided it withstands the reevaluation of the systematic uncertainties after the *Hitomi* result) will require the photon statistics comparable to that of the CCD stacking studies, or looking at objects where the line is easier to detect. Among clusters, such objects would be non-cool-core systems, in which the line EW should be an order of magnitude higher for the same line flux because of the lower ICM background. A DM line would be narrower, giving a calorimeter a greater leverage, in systems with low velocity dispersion, such as dwarf spheroidals and the Milky Way. Of course, distinguishing a DM line from an astrophysical one would require resolving the line, which only a calorimeter can do.

References

Abazajian, K., Fuller, G. M., & Tucker, W. H. 2001, ApJ, 562, 593
Abazajian, K. N., Acero, M. A., Agarwalla, S. K., et al. 2012, arxiv:1204.5379
Anderson, M. E., Churazov, E., & Bregman, J. N. 2015, MNRAS, 452, 3905
Boyarsky, A., Franse, J., Iakubovskyi, D., & Ruchayskiy, O. 2015, PhRvL, 115, 161301
Boyarsky, A., Iakubovskyi, D., & Ruchayskiy, O. 2012, PDU, 1, 136
Boyarsky, A., Ruchayskiy, O., Iakubovskyi, D., & Franse, J. 2014, PhRvL, 113, 251301
Bulbul, E., Markevitch, M., Foster, A., et al. 2014, ApJ, 789, 13 (B14)
Bulbul, E., Markevitch, M., Foster, A., et al. 2016, ApJ, 831, 55
Cash, W. 1979, ApJ, 228, 939
Churazov, E., Forman, W., Jones, C., & Böhringer, H. 2003, ApJ, 590, 225
Dodelson, S., & Widrow, L. M. 1994, PhRvL, 72, 17
Fabian, A. C., Walker, S. A., Pinto, C., Russell, H. R., & Edge, A. C. 2015, MNRAS, 451, 3061
Foster, A., Smith, R., & Brickhouse, N. 2012, ApJ, 756, 128

Franse, J., Bulbul, E., Foster, A., et al. 2016, ApJ, 829, 124 (F16)
Gross, E., & Vitells, O. 2010, EPJC, 70, 525
Gu, L., Kaastra, J., Raassen, A. J. J., et al. 2015, A&A, 584, L11
Henke, B. L., Gullikson, E. M., & Davis, J. C. 1993, ADNDT, 54, 181
Hitomi Collaboration, 2016, Natur, 535, 117 (H16)
Iakubovskyi, D. 2015, AASP, 6, 3
Kaastra, J. S., & Bleeker, J. A. M. 2016, A&A, 587, A151
Kalberla, P. M. W., Burton, W. B., Hartmann, D., et al. 2005, A&A, 440, 775
Kelley, R. L., Akamatsu, H., Azzarello, P., et al. 2016, Proc. SPIE, 9905, 99050V
Kent, S. M., & Sargent, W. L. W. 1983, AJ, 88, 697
Kurashima, S., Furuzawa, A., Sato, T., et al. 2016, Proc. SPIE, 9905, 99053Y
Lodders, K. 2003, ApJ, 591, 1220
Okajima, T., Soong, Y., Serlemitsos, P., et al. 2016, Proc. SPIE, 9905, 99050Z
Protassov, R., van Dyk, D. A., Connors, A., Kashyap, V. L., & Siemiginowska, A. 2002, ApJ, 571, 545
Ruchayskiy, O., Boyarsky, A., Iakubovskyi, D., et al. 2016, MNRAS, 460, 1390
Schmidt, R. W., Fabian, A. C., & Sanders, J. S. 2002, MNRAS, 337, 71
Sekiya, N., Yamasaki, N. Y., & Mitsuda, K. 2016, PASJ, 68, S31
Simionescu, A., Allen, S. W., Mantz, A., et al. 2011, Sci, 331, 1576
Soong, Y., OKajima, T., Serlemitsos, P. J., et al. 2014, Proc. SPIE, 9144, 914428
Struble, M. F., & Rood, H. J. 1999, ApJS, 125, 35
Takahashi, T., Mutsuda, K., Kelley, R., et al. 2014, Proc. SPIE, 9144, 914425
Takahashi, T., Kokubun, M., Mitsuda, K., et al. 2016, Proc. SPIE, 9905, 99050U
Tamura, T., Iizuka, R., Maeda, Y., Mitsuda, K., & Yamasaki, N. Y. 2015, PASJ, 67, 23
Urban, O., Werner, N., Allen, S. W., et al. 2015, MNRAS, 451, 2447
Vikhlinin, A., Kravtsov, A., Forman, W., et al. 2006, ApJ, 640, 691

AUTHORS

F. A. Aharonian[1,2], H. Akamatsu[3], F. Akimoto[4], S. W. Allen[5,6,7], L. Angelini[8], K. A. Arnaud[8,9], M. Audard[10], H. Awaki[11], M. Axelsson[12], A. Bamba[13], M. W. Bautz[14], R. D. Blandford[5,6,7], E. Bulbul[14], L. W. Brenneman[15], G. V. Brown[16], E. M. Cackett[17], M. Chernyakova[1], M. P. Chiao[8], P. Coppi[18], E. Costantini[3], J. de Plaa[3], J.-W. den Herder[3], C. Done[19], T. Dotani[20], K. Ebisawa[20], M. E. Eckart[8], T. Enoto[21,22], Y. Ezoe[12], A. C. Fabian[17], C. Ferrigno[10], A. R. Foster[15], R. Fujimoto[23], Y. Fukazawa[24], A. Furuzawa[25], M. Galeazzi[26], L. C. Gallo[27], P. Gandhi[28], M. Giustini[3], A. Goldwurm[29], L. Gu[3], M. Guainazzi[20,30], Y. Haba[31], K. Hagino[20], K. Hamaguchi[8,32], I. Harrus[8,32], I. Hatsukade[33], K. Hayashi[20], T. Hayashi[4], K. Hayashida[34], J. Hiraga[35], A. E. Hornschemeier[8], A. Hoshino[36], J. P. Hughes[37], Y. Ichinohe[12], R. Iizuka[20], H. Inoue[20], S. Inoue[34], Y. Inoue[20], K. Ishibashi[4], M. Ishida[20], K. Ishikawa[20], Y. Ishisaki[12], M. Itoh[38], M. Iwai[20], N. Iyomoto[39], J. S. Kaastra[3], T. Kallman[8], T. Kamae[5], E. Kara[9], J. Kataoka[40], S. Katsuda[41], J. Katsuta[24], M. Kawaharada[42], N. Kawai[43], R. L. Kelley[8], D. Khangulyan[36], C. A. Kilbourne[8], A. L. King[5,6], T. Kitaguchi[24], S. Kitamoto[36], T. Kitayama[44], T. Kohmura[45], M. Kokubun[20], S. Koyama[20], K. Koyama[46], P. Kretschmar[30], H. A. Krimm[8,47], A. Kubota[48], H. Kunieda[4], P. Laurent[29], F. Lebrun[29], S.-H. Lee[20], M. A. Leutenegger[8], O. Limousin[29], M. Loewenstein[8,9], K. S. Long[49], D. H. Lumb[50], G. M. Madejski[5,7], Y. Maeda[20], D. Maier[29], K. Makishima[51], M. Markevitch[8], H. Matsumoto[52], K. Matsushita[53], D. McCammon[54], B. R. McNamara[55], M. Mehdipour[3], E. D. Miller[14], J. M. Miller[56], S. Mineshige[21], K. Mitsuda[20], I. Mitsuishi[4], T. Miyazawa[57], T. Mizuno[24], H. Mori[8], K. Mori[33], H. Moseley[8], K. Mukai[8,32], H. Murakami[58], T. Murakami[23], R. F. Mushotzky[9], T. Nakagawa[20], H. Nakajima[34], T. Nakamori[59], T. Nakano[60], S. Nakashima[20], K. Nakazawa[13], K. Nobukawa[61], M. Nobukawa[62], H. Noda[63], M. Nomachi[64], S. L. O' Dell[65], H. Odaka[20], T. Ohashi[12], M. Ohno[24], T. Okajima[8], N. Ota[61], M. Ozaki[20], F. Paerels[66], S. Paltani[10], A. Parmar[50], R. Petre[8], C. Pinto[17], M. Pohl[10], F. S. Porter[8], K. Pottschmidt[8,32], B. D. Ramsey[65], C. S. Reynolds[9], H. R. Russell[17], S. Safi-Harb[67], S. Saito[36], K. Sakai[8], H. Sameshima[20], T. Sasaki[53], G. Sato[20], K. Sato[53], R. Sato[20], M. Sawada[68], N. Schartel[30], P. J. Serlemitsos[8], H. Seta[12], M. Shidatsu[51], A. Simionescu[20], R. K. Smith[15], Y. Soong[8], Ł. Stawarz[69], Y. Sugawara[20], S. Sugita[43], A. E. Szymkowiak[18], H. Tajima[70], H. Takahashi[24], T. Takahashi[20], S. Takeda[71], Y. Takei[20], T. Tamagawa[60], K. Tamura[4], T. Tamura[20], T. Tanaka[46], Yasuo Tanaka[20], Yasuyuki Tanaka[24], M. Tashiro[72], Y. Tawara[4], Y. Terada[72], Y. Terashima[11], F. Tombesi[8], H. Tomida[20], Y. Tsuboi[41], M. Tsujimoto[20], H. Tsunemi[34], T. Tsuru[46], H. Uchida[46], H. Uchiyama[73], Y. Uchiyama[36], S. Ueda[20], Y. Ueda[21], S. Ueno[20], S. Uno[74], C. M. Urry[18], E. Ursino[26], C. P. de Vries[3], S. Watanabe[20], N. Werner[75,76], D. R. Wik[8,77], D. R. Wilkins[27], B. J. Williams[8], S. Yamada[12], H. Yamaguchi[8], K. Yamaoka[4], N. Y. Yamasaki[20], M. Yamauchi[33], S. Yamauchi[61], T. Yaqoob[32,8], Y. Yatsu[43], D. Yonetoku[23], A. Yoshida[67], I. Zhuravleva[5,6], and A. Zoghbi[56]

[1] Astronomy and Astrophysics Section, Dublin Institute for Advanced Studies, Dublin 2, Ireland
[2] National Research Nuclear University (MEPHI), Moscow, 115409, Russia
[3] SRON Netherlands Institute for Space Research, Utrecht, The Netherlands
[4] Department of Physics, Nagoya University, Aichi 464-8602, Japan;
[5] Kavli Institute for Particle Astrophysics and Cosmology, Stanford University, Stanford CA 94305, USA
[6] Department of Physics, Stanford University, Stanford, CA 94305, USA
[7] SLAC National Accelerator Laboratory, Menlo Park, CA 94025, USA
[8] NASA/Goddard Space Flight Center, Greenbelt, MD 20771, USA;
[9] Department of Astronomy, University of Maryland, College Park, MD 20742, USA
[10] Université de Genève, 1211 Genève 4, Switzerland
[11] Department of Physics, Ehime University, Ehime 790-8577, Japan
[12] Department of Physics, Tokyo Metropolitan University, Tokyo 192-0397, Japan
[13] Department of Physics, University of Tokyo, Tokyo 113-0033, Japan
[14] Kavli Institute for Astrophysics and Space Research, Massachusetts Institute of Technology, Cambridge, MA 02139, USA

[15] Smithsonian Astrophysical Observatory, Cambridge, MA 02138, USA
[16] Lawrence Livermore National Laboratory, Livermore, CA 94550, USA
[17] Institute of Astronomy, Cambridge University, Cambridge CB3 0HA, UK
[18] Yale Center for Astronomy and Astrophysics, Yale University, New Haven, CT 06520, USA
[19] Department of Physics, University of Durham, Durham DH1 3LE, UK
[20] Institute of Space and Astronautical Science (ISAS), Japan Aerospace Exploration Agency (JAXA), Sagamihara, Kanagawa 252-5210, Japan
[21] Department of Astronomy, Kyoto University, Kyoto 606-8502, Japan
[22] The Hakubi Center for Advanced Research, Kyoto University, Kyoto 606-8302, Japan
[23] Faculty of Mathematics and Physics, Kanazawa University, Ishikawa 920-1192, Japan
[24] Department of Physical Science, Hiroshima University, Hiroshima 739-8526, Japan
[25] Fujita Health University, Toyoake, Aichi 470-1192, Japan
[26] Physics Department, University of Miami, Coral Gables, FL 33124, USA
[27] Department of Astronomy and Physics, Saint Mary's University, Halifax, NS B3H 3C3, Canada
[28] Department of Physics and Astronomy, University of Southampton, Highfield, Southampton SO17 1BJ, UK
[29] IRFU/Service d'Astrophysique, CEA Saclay, F-91191 Gif-sur-Yvette Cedex, France
[30] European Space Agency (ESA), European Space Astronomy Centre (ESAC), Madrid, Spain
[31] Department of Physics and Astronomy, Aichi University of Education, Aichi 448-8543, Japan
[32] Department of Physics, University of Maryland, Baltimore County, Baltimore, MD 21250, USA
[33] Department of Applied Physics and Electronic Engineering, University of Miyazaki, Miyazaki 889-2192, Japan
[34] Department of Earth and Space Science, Osaka University, Osaka 560-0043, Japan
[35] Department of Physics, School of Science and Technology, Kwansei Gakuin University, Hyogo 669-1337, Japan
[36] Department of Physics, Rikkyo University, Tokyo 171-8501, Japan
[37] Department of Physics and Astronomy, Rutgers University, Piscataway, NJ 08854, USA
[38] Faculty of Human Development, Kobe University, Hyogo 657-8501, Japan
[39] Kyushu University, Fukuoka 819-0395, Japan
[40] Research Institute for Science and Engineering, Waseda University, Tokyo 169-8555, Japan
[41] Department of Physics, Chuo University, Tokyo 112-8551, Japan
[42] Tsukuba Space Center (TKSC), Japan Aerospace Exploration Agency (JAXA), Ibaraki 305-8505, Japan
[43] Department of Physics, Tokyo Institute of Technology, Tokyo 152-8551, Japan
[44] Department of Physics, Toho University, Chiba 274-8510, Japan
[45] Department of Physics, Tokyo University of Science, Chiba 278-8510, Japan
[46] Department of Physics, Kyoto University, Kyoto 606-8502, Japan
[47] Universities Space Research Association, Columbia, MD 21046, USA
[48] Department of Electronic Information Systems, Shibaura Institute of Technology, Saitama 337-8570, Japan
[49] Space Telescope Science Institute, Baltimore, MD 21218, USA
[50] European Space Agency (ESA), European Space Research and Technology Centre (ESTEC), 2200 AG Noordwijk, The Netherlands
[51] RIKEN, Saitama 351-0198, Japan
[52] Kobayashi-Maskawa Institute, Nagoya University, Aichi 464-8602, Japan
[53] Department of Physics, Tokyo University of Science, Tokyo 162-8601, Japan
[54] Department of Physics, University of Wisconsin, Madison, WI 53706, USA
[55] University of Waterloo, Waterloo, ON N2L 3G1, Canada
[56] Department of Astronomy, University of Michigan, Ann Arbor, MI 48109, USA
[57] Okinawa Institute of Science and Technology Graduate University (OIST), Okinawa 904-0495, Japan
[58] Department of Information Science, Faculty of Liberal Arts, Tohoku Gakuin University, Miyagi 981-3193, Japan
[59] Department of Physics, Faculty of Science, Yamagata University, Yamagata 990-8560, Japan
[60] RIKEN Nishina Center, Saitama 351-0198, Japan
[61] Department of Physics, Faculty of Science, Nara Women's University, Nara 630-8506, Japan
[62] Department of Teacher Training and School Education, Nara University of Education, Takabatake-cho, Nara 630-8528, Japan
[63] The Frontier Research Institute for Interdisciplinary Sciences, Tohoku University, Sendai, Miyagi 980-8578, Japan
[64] Research Center for Nuclear Physics (Toyonaka), Osaka University, 1-1 Machikaneyama-machi, Toyonaka, Osaka 560-0043, Japan
[65] NASA/Marshall Space Flight Center, Huntsville, AL 35812, USA
[66] Department of Astronomy, Columbia University, New York, NY 10027, USA
[67] Department of Physics and Astronomy, University of Manitoba, Winnipeg, MB R3T 2N2, Canada
[68] Department of Physics and Mathematics, Aoyama Gakuin University, Kanagawa 252-5258, Japan
[69] Astronomical Observatory, Jagiellonian University, 30-244 Kraków, Poland
[70] Institute of Space-Earth Environmental Research, Nagoya University, Aichi 464-8601, Japan
[71] Advanced Medical Instrumentation Unit, Okinawa Institute of Science and Technology Graduate University (OIST), Okinawa 904-0495, Japan
[72] Department of Physics, Saitama University, Saitama 338-8570, Japan
[73] Science Education, Faculty of Education, Shizuoka University, Shizuoka 422-8529, Japan
[74] Faculty of Health Science, Nihon Fukushi University, Aichi 475-0012, Japan
[75] MTA-Eötvös University Lendület Hot Universe Research Group, Budapest 1117, Hungary
[76] Department of Theoretical Physics and Astrophysics, Faculty of Science, Masaryk University, 611 37 Brno, Czech Republic
[77] Department of Physics and Astronomy, Johns Hopkins University, Baltimore, MD 21218, USA